# A Transition in the Ni$^{2+}$ Complex Structure from Six- to Four-Coordinate upon Formation of Ion Pair Species in Supercritical Water:  An X-ray Absorption Fine Structure, Near-Infrared, and Molecular Dynamics Study

**Markus M. Hoffmann, John G. Darab, Bruce J. Palmer, and John L. Fulton***

*Environmental and Energy Sciences Division, Pacific Northwest National Laboratory,[†] Richland, WA 99352*

*Received: February 5, 1999; In Final Form: July 7, 1999*

The coordination structure about Ni$^{2+}$ in water at temperatures up to 525 °C was measured by the X-ray absorption fine structure (XAFS) technique. Solutions containing 0.2 *m* NiBr$_2$ and 0.2 *m* NiBr$_2$/0.8 *m* NaBr were explored at pressures up to 720 bar. For certain systems, both Ni *and* Br XAFS data were acquired and a global model was used to fit the two independent sets of XAFS data. These two independent measurements gave excellent agreement on the coordination structure of the Ni$^{2+}$/Br$^-$ contact-ion pairing. The result is a complete picture of the coordination structure of the contact-ion pairing including the coordination numbers, distances for the water−ion and ion−ion associations, and also a high-quality measurement of the binding strength and amount of disorder (Debye−Waller factor and the anharmonicity) of the Ni$^{2+}$/Br$^-$ association. The XAFS measurements strongly indicate a transitional change in the coordination of Ni$^{2+}$ from the octahedral Ni$^{2+}$(H$_2$O)$_6$ species at room temperature to the 4-coordinate structures at supercritical conditions (e.g., *T* > 375 °C). Specifically, the equilibrium structure at 425 °C is Ni$^{2+}$(Br$^-$)$_{3.3}$(H$_2$O)$_{1.0}$ for the aqueous solution of 0.2 *m* NiBr$_2$ with 0.8 *m* NaBr. At 325 °C, the octahedral species still exists but it is in equilibrium with new species of lower coordination. Above 425 °C, at moderate pressures up to 700 bar, the stable structures are a family of 4-coordinated species (NiBr(H$_2$O)$_3$·Br, NiBr$_2$(H$_2$O)$_2$, NiBr$_3$(H$_2$O)·Na), where the degree of Br$^-$ adduction and replacement of H$_2$O in the inner shell depends on the overall Br$^-$ concentration. The most likely symmetry of these species is a distorted tetrahedron. Measurements of the Ni preedge 1$s \rightarrow$ 3$d$ and to 1$s \rightarrow$ 4$d$ transitions using X-ray absorption spectroscopy confirm that a symmetry change occurs at high temperature, and the results are consistent with the XAFS and molecular dynamics (MD) conclusion of a distorted tetrahedral structure. This observation is further confirmed by near-infrared (NIR) spectra of the same system. The MD simulations under identical conditions were used to verify the experimental findings. Although we found qualitative agreement between the experimental and simulated first-shell coordination structure, it is clear that refinements of the intermolecular potentials are required to quantitatively capture the true high-temperature structure.

## Introduction

In aqueous solutions at high temperatures, cations and anions that would normally be fully dissociated under ambient conditions start to associate into a multitude of different ion-pair structures. These ions undergo dramatic reductions in the extent of hydration as the ion pairs form in lower density water where the breakup of the hydrogen-bonding structure[1] at higher temperatures leads to a much lower dielectric constant (low frequencies). The low dielectric constant limits the ability of the solvent to screen attractive electrostatic interactions. Thus, a high degree of ion association occurs at temperatures above the critical point of water (375 °C). In addition to the purely electrostatic forces driving the association of cations and anions, when the cation is a transition metal, there are chemical effects because there are significant energy differences between the molecular orbitals of the various transition metal complexes. Results from theoretical and simulation work have revealed a great deal about the ion pairing phenomena[2,3] although there are still large uncertainties about the validity of the intermo-

lecular potentials (especially ion−ion potentials) that have mostly been parametrized using ambient temperature data. Some experimental evidence[4−6] of the existence of ion pairing was also derived from electronic and Raman spectroscopy but yielded little direct structural information. Earlier ultraviolet− visible (UV−vis) spectroscopic studies by Lüdemann et al.[7] showed clear evidence of symmetry changes about the Ni$^{2+}$ cation for an aqueous NiCl$_2$/NaCl solution up to 500 °C. Another UV−vis study to 300 °C, with only NiBr$_2$ present in the aqueous solution, showed thermochromic spectral shifts but no convincing evidence of symmetry changes at this temperature.[8]

Many recent studies[9−14] have exploited X-ray absorption fine structure (XAFS) for in situ studies of hydrothermal systems (including the supercritical region), and the realization is that this technique gives quantitative information on the structure of the first solvation shell about ionic species in these high-temperature solutions. In previous studies,[12] we reported the first detailed structural characterization of a contact-ion pair under supercritical water conditions. In this report, we explore in more detail the nature of the changes in Ni$^{2+}$ coordination at high salt concentrations. To this end, we conduct separate XAFS measurements on *both* the cation (Ni K-edge) and the anion (Br K-edge) in the same solution under identical conditions. A

* Corresponding author. E-mail: jl_fulton@pnl.gov. FAX: 509-376-7011.
† Operated by Battelle Memorial Institute.

global fit of these two data sets provides high confidence in the measured parameters. Further, we examine transitions in the X-ray absorption preedge structure and the near-infrared (NIR) spectra that provide clear evidence of symmetry changes. Finally, we use molecular dynamics (MD) simulation to validate the methods of XAFS analysis and then to test the performance of the various intermolecular potentials under high-temperature conditions.

## Experimental Section

The experimental technique that has been utilized for the acquisition of XAFS spectra under high-pressure, high-temperature conditions was slightly revised from previous studies[9,11,15] and has recently been described in much detail.[16] The important aspects are briefly summarized here. The synthetic diamond X-ray windows (single crystal for Ni XAFS and polycrystalline for Br XAFS) were mounted in such a way as to provide a 2.5-mm path length. For the polycrystalline windows, a background scan of pure water at the identical conditions is subtracted from the sample spectra to remove small window contributions. This procedure is not necessary for the single-crystal diamond windows where the window contributions to the spectrum were absent over the acquired energy range. The body of the cell and the transfer lines were constructed from a Pt/Ir (90%/10%) alloy that provides high corrosion resistance for these solutions. A high degree of temperature uniformity within the cell was achieved by covering it with multiple layers of a thermal radiation barrier material and then placing it inside a vacuum chamber. High-temperature uniformity is essential to eliminate fluid density fluctuations that impair the acquisition of XAFS in the high $k$-region. It is essential to acquire XAFS spectra to at least $k = 12$ Å$^{-1}$ so that the effects of disorder and anharmonicity in the pair distribution function can be properly determined. The temperature of the cell was maintained to within $\pm 1$ °C with a three-mode controller (Omega, no. CN3000) with platinum resistive probes, whereas the fluid pressure was measured to within $\pm 1$ bar with an electronic transducer (Precise Sensors, Inc., no. D451). The NIR spectra were acquired in the same cell used for the XAFS measurements on a Bruker IFS 66v Fourier transform infrared (FT-IR) spectrometer at 5.0 cm$^{-1}$ resolution.

The nickel $K$-edge (8333 eV) and bromine $K$-edge (13 474 eV) XAFS spectra were collected on the insertion device beamline (PNC−CAT) at the Advanced Photon Source (APS; Argonne National Laboratory) and on the beamline X-19A of the National Synchrotron Light Source (NSLS; Brookhaven National Laboratory). The spectra obtained from NSLS are typically the average of three 20-min scans, whereas a single scan was sufficient to obtain high-quality spectra at APS. The optical setup and tuning were identical to those previously reported.[12] Energy calibration was accomplished with a Ni foil for the Ni-edge and NiBr$_2$ for the Br-edge. Only the single-phase region was explored for all conditions of this study. In this case, the solution densities under all conditions can be conveniently and accurately determined from the height of the nickel absorption edge.[11] All spectra were acquired under conditions of constant molal concentrations. The anhydrous NiBr$_2$ and NaBr had reported purities of 99% and were used as received from Alfa Aesar. All solutions were deoxygenated by purging with N$_2$ prior to use. We concluded that the likelihood of nickel hydrolysis at 425 °C was relatively insignificant for this unbuffered system. First, the p$K$ values for Ni$^{2+}$ are relatively high.[17] Second, the starting pH (3.5) of the nickel solution is very low, and formation of trace amounts of

Ni((OH)(OH$_2$)$_n$)$^{-1}$ would further lower the pH, favoring the aqua-cation, Ni$^{2+}$(H$_2$O)$_6$.

The methods for data collection, background correction, and data transformation are well established.[18−20] The XAFS oscillations, $\chi(k)$, were extracted from the experimentally measured absorption coefficient by an automated background subtraction method (AUTOBK) developed by Newville et al.[21] in which the wavenumber of the ejected photoelectron is given by $k = \sqrt{2m_e(E-E_0)/\hbar^2}$ with $E_0$ being the absorption edge energy. The implementation of AUTOBK for the Ni and Br systems has previously been described.[12,15]

The analysis of the XAFS $\chi(k)$ function was based on the XAFS relationship given by

$$\chi(k) = \frac{F(k)S_0^2 N}{kR^2}e^{-2k^2\sigma^2}e^{-2R/\lambda(k)}\sin\left(2kR + \delta(k) - \frac{4}{3}k^3C_3\right) \quad (1)$$

where $F(k)$, $\delta(k)$, and $\lambda(k)$ are the amplitude, phase, and mean-free path factor, respectively, that are derived from the theoretical standards calculated using an ab initio, multiple scattering XAFS code (FEFF).[22] We used a core-hole factor of $S_0^2 = 0.85$ for Ni that is reported to be accurate to within ~20%.[23−25] This $S_0^2$ value was verified by FEFF, fitting to the two solid standards Ni(OH)$_2$ and NiBr$_2$. For Br$^{-1}$ we use the value of $S_0^2 = 0.91$ that has been previously measured by Frenkel et al.[26] The remaining terms in eq 1 are $N$, the coordination number of the shell, $R$, the shell distance, $\sigma^2$, the Debye−Waller factor that represents the mean-square variation in $R$ due to both static and thermal disorder, and finally $C_3$, the anharmonicity of the pair distribution. The parameter $C_3$ is a measure of the asymmetry of the peaks in the pair distribution function $G_{ij}(r)$ between two atoms $i$ and $j$. For a completely symmetric peak (e.g., a perfect Gaussian), $C_3$ vanishes, but as the peak becomes more asymmetric, the value of $C_3$ increases. The parameters descibed in eq 1, that contain the quantitative structural information were determined with an analysis program (FEFFIT)[27] that employs a nonlinear, least-squares fit to the theoretical standards calculated by FEFF. In addition to the structural parameters, a single nonstructural parameter, $\Delta E_0$, is varied to account for the simple estimate of $E_0$ made by FEFF.

The FEFF calculations for Ni−O were done with atomic configurations based on the crystallographic structure[28,29] of Ni(OH)$_2$. The Ni $\chi(k)$ data were weighted by $k^2$, and windowed between $2.0 < k < 12.0$ Å$^{-1}$ using a Hanning window with $dk = 1.0$ Å$^{-1}$. The fits were done on both the real and imaginary parts of $\tilde{\chi}(R)$ in the region of $1.4 < R < 4.2$ Å. For Br$^-$, the detailed procedures for removing the multielectron excitations and the treatment of the amplitude function at low $k$ values have previously been described.[15] The FEFF calculations for Br−O were done with atomic configurations based on the crystallographic structure of NaBrO$_3$.[30] The Br $\chi(k)$ data were weighted by $k^2$, and windowed between $1.75 < k < 12.0$ Å$^{-1}$ using a Hanning window with $dk = 1.0$. Typical plots of the Ni$^{2+}$ and Br$^-$ XAFS spectra, their corresponding background functions, the $k^2$-weighted $\chi(k)$ plots, and $R$-space plots for the data and the fits to the theoretical standard are given in the Supporting Information supplied in earlier publications.[12,15] The uncertainties reported later (Tables 2−4) correspond to an increase in the misfit between the data and the best fit model by an amount of $1/\nu$, where $\nu$ is the degrees of freedom in the fit (typically, $\nu = 2$ for the Br$^-$ data).

In addition to single-scattering paths accounting for the Ni−O, Ni−Br, and Br−O structure, the fitting to the Ni$^{2+}$ included three linear, multiple-scattering (MS) paths (O−Ni−O) for the

Ni²⁺ Complex Structure Transition in Supercritical Water

*J. Phys. Chem. A, Vol. 103, No. 42, 1999* **8473**

**TABLE 1: Pair Potential Parameters for the MD Simulations**

| atom | $\sigma$, Å | $\epsilon$, (kcal/mol) | $q(|e|)$ |
|------|------|------|------|
| O | 3.169 | 0.1553 | −0.8476 |
| H | 0.000 | 0.0000 | 0.4238 |
| Ni[a] | 2.050 | 0.1000 | 2.0000 |
| Br[a] | 4.686 | 0.1000 | −1.0000 |
| Na | 2.584 | 0.1000 | 1.0000 |

[a] The Ni−Br Lennard-Jones radius was optimized to 3.18 Å to match the experimental result under supercritical conditions.

octahedral structure that accounted for a small peak in the *R*-space plot occurring at ~3.5 Å (vide infra). Inclusion of the MS paths did not significantly affect the fits of the variables to the first shell because the distances of the MS paths are twice those of the single-scattering paths. At higher temperatures, the disorder is high enough so that the MS paths are no longer significant. One additional single-scattering path accounting for the contact-ion pairing was included for fits to the spectra at elevated temperature. Further, the inclusion of a Br−Na scattering path for the Br XAFS at high temperatures did not improve the fit to the experimental data most likely because of the interference of the neighboring oxygens. There is no evidence of ion pair formation at ambient conditions.

For certain conditions at 425 °C, both Ni and Br XAFS were acquired on the same system. In this case, a global model was used to *simultaneously* fit both data sets. In this instance, the following linear paths were included: Ni−O, Ni−Br, Br−O, and Br−Ni. For the Ni−Br and Br−Ni paths, the number of nearest neighbors are constrained by the relationship given in eq 4. In addition, *R*, $\sigma^2$, and $C_3$ for these paths are the same.

## Simulation Methods

The methods that were used to obtain simulated XAFS spectra from the MD simulations have been previously described.[10,12,15] Simulations of the nickel bromide/sodium bromide system at 697 K were performed using the extended simple point charge model (SPC/E) for water.[31] Parameters for nickel were developed as part of this study and parameters for bromide and sodium ion were obtained from Dang.[32,33] The SPC/E model consists of pairwise interactions between all atomic sites of the following form

$$\phi_{ij}(r_{ij}) = 4\epsilon_{ij}\left[\left(\frac{\sigma_{ij}}{r_{ij}}\right)^{12} - \left(\frac{\sigma_{ij}}{r_{ij}}\right)^6\right] - a_{ij} - b_{ij}(r_c - r_{ij}) + \frac{q_i q_j}{r_{ij}}$$
$$r_{ij} < r_c \quad (2)$$

$$\phi_{ij}(r_{ij}) = \frac{q_i q_j}{r_{ij}} \qquad r_{ij} \geq r_c \quad (3)$$

The constants $a_{ij}$ and $b_{ij}$ were chosen so that the potential and force due to the Lennard−Jones interaction (the first two terms in eq 2) vanish at the cutoff distance $r_c$. The cutoff was set at 8.5 Å for all simulations using this model. The long-range Coulomb interactions were handled using an Ewald summation. The parameters $\sigma_i$, $\epsilon_i$, and $q_i$ were defined for each atomic species *i*, and the parameters appearing in eq 2 were then obtained using the mixing rules $\epsilon_{ij} = \sqrt{\epsilon_i \epsilon_j}$ and $\sigma_{ij} = (\sigma_i + \sigma_j)/2$. All parameters used in these calculations are summarized in Table 1. The one exception to using the mixing rules was for the Ni−Br interaction. The parameter $\sigma_{ij}$ was changed from the mixing rule value of 3.368 Å to 3.18 Å to obtain better agreement between the experimental and simulated XAFS spectra. This adjustment was made in earlier studies[12] after initial

simulations showed large discrepancies between the equilibrium Ni−Br distances and those that were obtain in the experimental results.

All simulations consisted of 278 rigid water molecules plus 1 nickel, 4 sodium, and 6 bromide ions, corresponding to a 0.20 *m* solution of nickel bromide and a 0.8 *m* solution of NaBr. The system sizes were adjusted so that the density of the 697 K solution was 0.650 g/cm³. The temperature was controlled with simple velocity scaling, and the equations of motion were integrated with the velocity Verlet algorithm recast as a 3-point Gear predictor−corrector.[34] The rigid geometry of the water molecules was maintained with a variant of the SHAKE algorithm.[35] Each trajectory was run for a total of 50 ps using a 2.5-fs time step.

Every 0.2 ps, a configuration from the simulation was saved to a file, resulting in a total of 250 configurations for each simulation. Several clusters were extracted from each configuration, with one for the nickel atom and one for each bromine atom. Each cluster contained the central atom (Ni²⁺ or Br⁻) plus all other atoms, except hydrogen, falling within a cutoff distance, $R_c$ of the central atom. For nickel, the cutoff distance was set at 5 Å. For bromine the effects of the cutoff at 5 Å were still apparent, so $R_c$ was increased to 6 Å. These clusters were used as input for a calculation of the nickel XAFS spectrum using the FEFF6 multiple-scattering code. The 250 individual nickel spectra and the 1500 individual bromine spectra were then separately averaged together to obtain a solvent-averaged Ni and Br MD-XAFS spectra that could then be compared directly with the spectra obtained from the XAFS experiments.[10]

## Results

There are three different experimental XAFS data sets that are described in the following sections. The first and second data sets contain both Ni *and* Br XAFS data for a single thermodynamic condition that were analyzed with a single global model. One of these solutions is aqueous 0.2 *m* NiBr₂ (425 °C, 450 bar, 0.54 g/cm³) and the other is aqueous 0.2 *m* NiBr₂/0.8 *m* NaBr (425 °C, 410 bar, 0.62 g/cm³). The third data set contains a temperature series from 25 to 525 °C, in which we use only Ni XAFS to explore the changes in the local nickel structure for a concentrated Br⁻ solution containing 0.2 *m* NiBr₂ and 0.8 *m* NaBr. This series is similar to previously reported data[12] for the system containing just 0.2 *m* NiBr₂, with the exception that in the new series the high Br⁻ concentration drives the equilibria strongly toward the tribromo nickel species. In the subsequent results section, MD simulations are used to generate XAFS spectra that are directly compared to the experiment results. This comparison tests various assumptions about the XAFS analysis techniques. In addition to the XAFS data, both the X-ray absorption preedge spectra and NIR spectra of these solutions are presented to substantiate the conclusions regarding the coordination changes that are observed using XAFS.

**XAFS Spectra and the Fitted Results.** Figures 1 and 2 present the Ni-edge *and* Br-edge *k*-weighted $\chi(k)$ plots at 425 °C and 450 bar for the NiBr₂ and NiBr₂/NaBr solutions, respectively. In all cases the usable *k*-range extends out to ~12 Å⁻¹. Because bromine is a much higher Z atom than the oxygen, the amplitude and phase functions [$F(k)$ and $\delta(k)$ in eq 1] derived from FEFF have significantly different features. The bromine $F(k)$ function has a large amplitude for $k > 5$ Å⁻¹, thus one can identify the approximate transition from the O (H₂O) contribution to a predominately Br contribution in the phase-shift region located around $k = 4-5$ Å⁻¹ in both Figures 1 and 2. The existence of significant XAFS oscillation out to $k = 12$
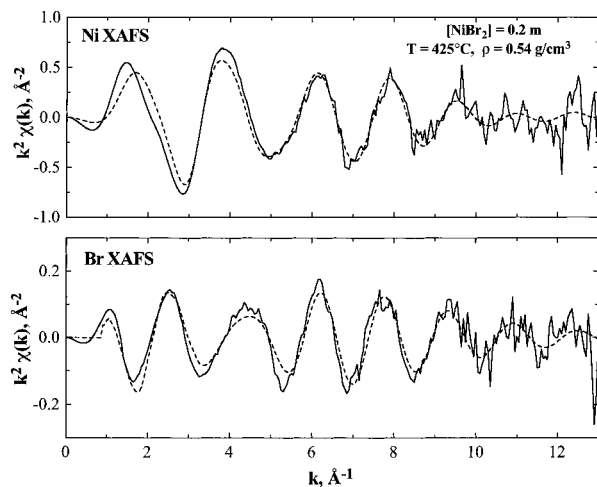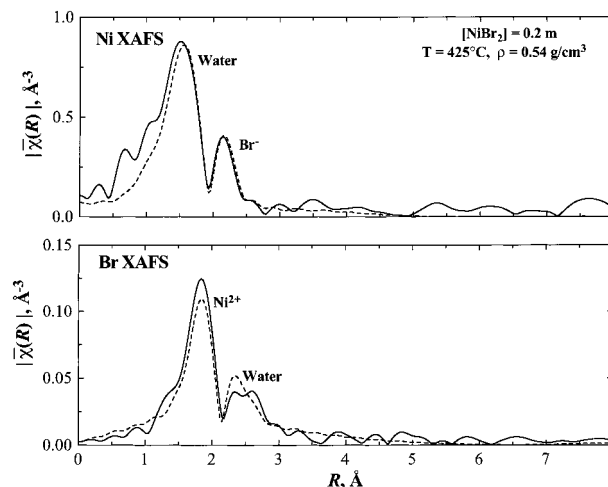
**Figure 1.** The *k*-weighted $\chi(k)$ plots for $Ni^{2+}$ and $Br^-$ XAFS under supercritical conditions for a 0.2 *m* $NiBr_2$ solution at 425 °C and 450 bar. The solid line shows the experimental data and the dashed line shows the global model fit to both data sets using FEFF calculations and the parameters listed in Table 2.
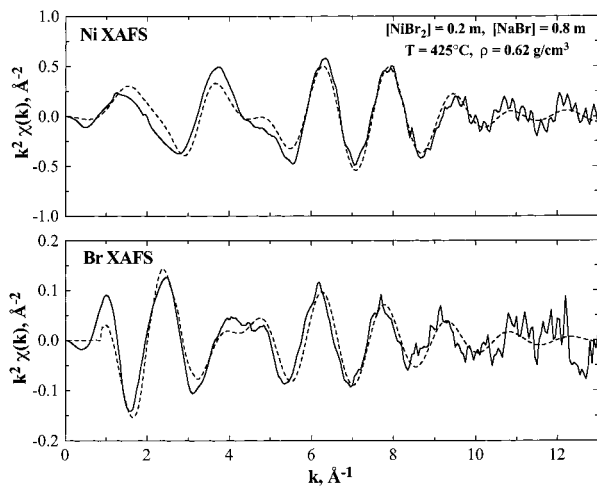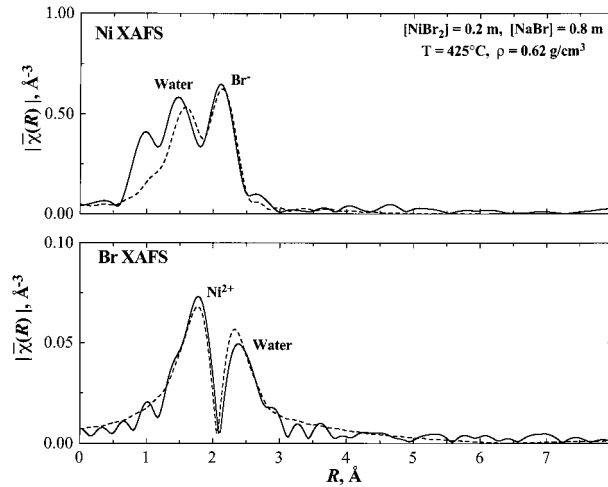


**Figure 2.** The *k*-weighted $\chi(k)$ plots for $Ni^{2+}$ and $Br^-$ XAFS under supercritical conditions for a 0.2 *m* $NiBr_2$ and 0.8 *m* NaBr solution at 425 °C and 410 bar. The solid line shows the experimental data and the dashed line shows the global model fit to both data sets using FEFF calculations and the parameters listed in Table 2.



**Figure 3.** The $|\tilde{\chi}(R)|$ plot from the 0.2 *m* $NiBr_2$ spectra shown in Figure 1 at 425 °C and 450 bar. The solid line shows the experimental data and the dashed line shows the global model fit using FEFF calculations and the parameters listed in Table 2. The $|\tilde{\chi}(R)|$ plot is uncorrected for phase shifts, whereas the corrected distances are reported in Table 2.



**Figure 4.** The $|\tilde{\chi}(R)|$ plot from the 0.2 *m* $NiBr_2$ and 0.8 *m* NaBr spectra shown in Figure 2 at 425 °C and 410 bar. The solid line shows the experimental data and the dashed line shows the global model fit using FEFF calculations and the parameters listed in Table 2. The $|\tilde{\chi}(R)|$ plot is uncorrected for phase shifts, whereas the corrected distances are reported in Table 2.

$Å^{-1}$ means that there is low disorder in the Ni–Br association and that this species is tightly bound because there is low damping from the Debye–Waller term (eq 1). At the higher temperatures, we would also expect to observe significant Br–Na ion pairing, although, as we will describe in subsequent sections, this species cannot be clearly differentiated from the Br–O structures using XAFS. Previously reported spectra[12,15] for low-temperature $NiBr_2$ solutions (25–200 °C) show that the amplitude of $\chi(k)$ oscillations is much larger than at high temperatures primarily because of the higher Ni–O coordination numbers. In addition, the presence of only water in the first shell at these low temperatures leads to a monomodal oscillation out to high *k*-values. At 25 °C, the previously reported spectra for both $Ni^{2+}$ and $Br^-$ [12,15] are consistent with the first-shell coordination involving 6 waters in a pure octahedral structure for the $Ni^{2+}$ and ~7 associated waters for the $Br^-$.

Figures 3 and 4 present the corresponding $\tilde{\chi}(R)$ plots from the transformed $\chi(k)$ data of the two different nickel solutions at 425 °C shown in Figures 1 and 2, respectively. These figures illustrate the probability of finding a particular atom at a certain distance from the central scattering atom. The $\tilde{\chi}(R)$ functions

are closely related to a standard radial distribution function. The plots clearly show the positions and relative numbers of nearest-neighbor atoms around the $Ni^{2+}$ and the $Br^-$ ions. When comparing the local $Ni^{2+}$ structure in Figure 4 to that in Figure 3, it is apparent that there is a large increase in the $Br^-$ coordination and a reduction in the $H_2O$ coordination for the system containing the high concentration of NaBr. For the Ni XAFS $\tilde{\chi}(R)$ plot in Figure 4, the peak at 0.9 Å is an artifact at an unrealistically short distance arising from the Fourier transform of the $\chi(k)$ that most likely contains a residual contribution from the background function. From the $Br^-$ $\tilde{\chi}(R)$ plot, the amplitude of the Ni peak actually decreases for the system with added NaBr even though the amount of coordination with Ni increases. This result is due to a large amount of the added $Br^-$ (from the NaBr salt) that is not associating with the $Ni^{2+}$ but rather forms Na–Br ion pairs. The simple stoichiometric equation,

$$N_{Ni} = N_{Br}([Ni^{2+}]/[Br^-]) = N_{Br}([NiBr_2]/(2[NiBr_2]+[NaBr])) \tag{4}$$

**TABLE 2: Global Model Fit to *Both* Ni and Br XAFS Measurements [Results of XAFS analysis for the first-shell Ni²⁺ hydration, the first-shell Br⁻ hydration and for the NiBr$_n$ ion pairing under supercritical conditions. For the global fit, the relationship between the number of Br⁻ about Ni²⁺ ($N_{Br}$) and the number of Ni²⁺ about Br⁻ ($N_{Ni}$) is defined as $N_{Ni} = N_{Br}([Ni^{2+}]/[Br^-])$. Concentrations expressed in molality.]**

| Ni²⁺/H₂O interaction | | | Ni²⁺/Br⁻ interaction | | | | Br⁻/H₂O interaction | | | |
|---|---|---|---|---|---|---|---|---|---|---|
| $N_{H_2O}$ | $R$, Å | $\sigma^2 \times 10^3$, Å² | $N_{Br}$ | $R$, Å | $\sigma^2 \times 10^3$, Å² | $C_3 \times 10^4$ | $N_{H_2O}$ | $R$, Å | $\sigma^2 \times 10^3$, Å² | $R^a$ |
| *[NiBr₂] = 0.2 m, T = 425 °C, P = 450 bar, ρ = 0.54 g/cm³* | | | | | | | | | | |
| 2.4(0.4) | 2.088(09) | 6.7(3.1)$^b$ | 1.2(0.3) | 2.428(15) | 8.3(2.2) | 6.3(3.4) | 4.0(1.4) | 3.260(14) | 41.1(14.8)$^b$ | 0.018 |
| *[NiBr₂] = 0.2 m, [NaBr] = 0.8 m, T = 425 °C, P = 410 bar, ρ = 0.62 g/cm³* | | | | | | | | | | |
| 1.0(0.2) | 2.091(10) | 3.2(3.1)$^b$ | 3.3(0.6) | 2.405(12) | 12.2(1.5) | 1.2(2.9) | 4.3(1.3) | 3.315(14) | 43.3(12.5)$^b$ | 0.024 |

$^a$ Goodness of fit defined by a scaled sum of squares as described in FEFFIT.[27] $^b$ Due to the low extent of water coordination for this system, the third cumulant for Br–O was fixed at $C_3 \times 10^4 = 40.0$, based on previous measurements.[15] Likewise, the third cumulant for Ni–O was fixed at $C_3 \times 10^4 = 10.0$, based on previous measurements.[12]

**TABLE 3: Results of Ni XAFS Analysis of First-Shell Ni²⁺ Hydration and for the Ni²⁺/Br$_n$ Ion Pair Under Liquid and Supercritical Conditions [Concentrations expressed in molality are 0.2 *m* NiBr₂ and 0.8 *m* Na Br.]**

| conditions | | | Ni²⁺/H₂O interaction | | | | Ni²⁺/Br⁻ interaction | | | |
|---|---|---|---|---|---|---|---|---|---|---|
| $T$, °C | $P$, bar | $\rho$, g/cm³ | $N_{H_2O}$ | $R$, Å | $\sigma^2 \times 10^3$, Å² | $C_3 \times 10^4$ | $N_{Br}$ | $R$, Å | $\sigma^2 \times 10^3$, Å² | $R^a$ |
| 25 | 1 | 1.10 | 6.7 (0.5) | 2.052 (07) | 6.0 (1.0)$^b$ | 1.5 (2.1) | — | — | — | 0.019 |
| 200 | 100 | 1.01 | 6.1 (0.4) | 2.067 (12) | 8.1 (1.2)$^c$ | 1.7 (2.4) | — | — | — | 0.015 |
| 325 | 150 | 0.79 | 4.3 (0.4) | 2.084 (29) | 9.0 (2.0)$^d$ | 5.9 (3.6) | 0.5 (0.4) | 2.441 (17) | 6.3 (6.0) | 0.017 |
| 425 | 357 | 0.53 | 1.3 (0.4) | 2.063 (27) | 5.0 (5.0) | 8.0$^e$ | 4.3 (1.3) | 2.402 (07) | 13.5 (2.9) | 0.038 |
| 475 | 670 | 0.58 | 1.0 (0.5) | 2.056 (23) | 5.0 (8.0) | 8.0$^e$ | 3.8 (1.6) | 2.378 (10) | 14.2 (4.1) | 0.073 |
| 525 | 720 | 0.47 | 0.7 (0.3) | 2.051 (22) | 0.6 (6.5) | 8.0$^e$ | 3.9 (1.5) | 2.361 (09) | 13.8 (3.9) | 0.059 |

$^a$ Goodness of fit defined by a scaled sum of squares as described in FEFFIT.[27] $^b$ The MS paths (O–Ni–O) of the octahedral structure have $\sigma^2 \times 10^3 = 3.2(5.0)$ Å². $^c$ The MS paths have $\sigma^2 \times 10^3 = 9.6(6.4)$ Å². $^d$ The MS paths have $\sigma^2 \times 10^3 = 17.2(12.3)$ Å². At higher temperature, there is no significant contribution to these MS paths. $^e$ Fixed in the fitting because this spectra has higher noise due to lower water coordination. Value selected from previous system.[12] Fitted $k$ range is only from 2 to 10 Å⁻¹ for these temperatures.

describes the relationship between the number of Br⁻ about a Ni²⁺, $N_{Br}$, and the number of Ni²⁺ about a Br⁻, $N_{Ni}$, for *all* Ni²⁺ and Br⁻ in this system. This relationship was used in the global fit to the Ni and Br XAFS experimental data. As an example, for the system containing only NiBr₂, if the Ni XAFS measures 1 Br⁻ about the Ni²⁺, then the corresponding Br XAFS measurement on the same system would detect 0.5 Ni²⁺ about the Br⁻ because the second Br⁻ would be associating only with water and/or Na⁺.

The dashed lines in Figures 1−4 represent the results from the global model that was used to *simultaneously* fit the two different sets of XAFS spectra. There is truly remarkable agreement between this model and the experimental result, thus giving us very high confidence in the derived parameters for these two different concentrations at 425 °C. The tabulated values for all of the regressed parameters are reported in Table 2. The results contain a complete description of the average first-shell structure about Ni²⁺ and Br⁻, including a detailed description of the nature of the contact-ion pairing species, NiBr$_n^{(2-n)+}$. In Table 2, the Br⁻ parameters for the system that contains added NaBr, represents average H₂O coordination numbers for those Br⁻ that are associating with Ni²⁺ *and* those that are only associating with Na⁺.

Table 3 presents the Ni XAFS results for a series of temperatures from ambient to 525 °C for the 0.2 *m* NiBr₂ and 0.8 *m* NaBr solution. Although the uncertainties of the measured parameters are somewhat higher in these data, because there are no confirming Br XAFS data, the large changes in the local Ni²⁺ structure are well captured in this series. In particular, the extent of hydration drops from ∼6 waters at low temperatures to ∼1 water at elevated temperatures. The large reduction in the extent of hydration occurs over the same temperature interval that the contact-ion pairing occurs. Both of these aspects are well correlated with the measured changes in the fluid density that are also reported in Table 3.

In the XAFS spectra, there is still a significant O–Ni–O
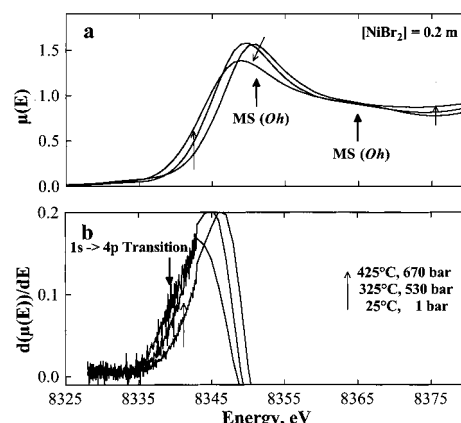


**Figure 5.** Preedge peaks of the Ni *K*-edge XANES spectra of the 0.2 *m* NiBr₂ solution at three temperatures from 25 to 425 °C. The spectra in (a) show the full range of data, whereas the derivative spectra are presented in (b). All spectra were scaled to a common edge-height. The energy resolution (eV) of these spectra is much lower than that of Figure 6. Heavy arrows mark positions of spectral features that are described in the text. Light arrows show the directions of change in the spectra with increasing temperature. In (b), the change in the noise character at 8343 is due to a change in the energy-step size of the X-ray monochromator during the spectral acquisition.

multiple-scattering contribution (two prominent features in the XANES region at 8352 and 8365 eV in Figures 5 and 6) at 325 °C, suggesting that even at this temperature there is still some amount of the octahedral, hexa-aqua Ni²⁺ species present (in equilibrium with a tetrahedral species). However, when the temperature is increased only another 100 °C higher to 425 °C, the multiple scattering is absent, suggesting that there is no octahedral species at this temperature. This interpretation was confirmed using FEFF simulations of Ni²⁺ structures with octahedral water coordination and for two different tetrahedral structures, one with tetrahedral water and the other a tetrahedral structure that contained 3 Br⁻ and 1 water (one of the proposed
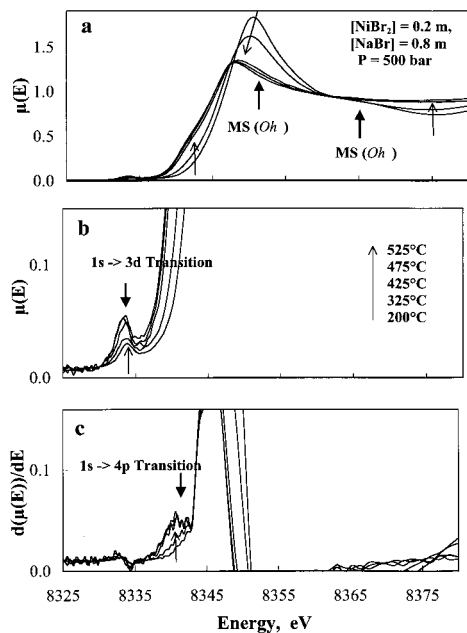
**Figure 6.** Preedge peaks of the Ni *K*-edge XANES spectra for the 0.2 *m* NiBr$_2$ and 0.8 *m* NaBr solution at five temperatures from 200 to 525 °C. The spectra in (a) show the full range of data, whereas in (b) the vertical scale is expanded to show the $1s \rightarrow 3d$ transition. The derivative spectra is shown in (c). All spectra were scaled to a common edge-height. Heavy arrows mark positions of spectral features that are described in the text. Light arrows show the directions of change in the spectra with increasing temperature.

high-temperature structures). In these simulations, we used a conservative (low) value of the Debye−Waller factor of 0.005 Å$^2$. The results clearly show that the linear MS paths of the octahedral structure have strong contributions in the XANES region, whereas the triangular MS paths from the tetrahedral structure are relatively weak. This result is especially true for the mixed (Br$^-$, H$_2$O) tetrahedral species because the redundancy of the MS paths is much lower than for the octahedral species. In addition, the amplitude factor (see eq 1) for higher Z atoms such as Br$^-$ is much lower than for O in the low *k* range from 0 to 4 Å$^{-1}$, which further reduces the contributions to the MS paths for these species.

From the tabulated data in Table 3 there are other structural features of the Ni$^{2+}$ solvation that are worthy of mention. The measured Ni−O distance does not change at high temperatures within the experimental error of about ±0.03 Å. For this NiBr$_2$/NaBr solution containing high Br$^-$ concentrations, the number of waters about the nickel is ∼1. This fact, and the dominance of the Br contribution to the Ni XAFS means that the measurements of the water disorder ($\sigma^2$ and $C_3$) about Ni$^{2+}$ is more difficult. For the system containing only NiBr$_2$, the measurement of the water disorder is much easier because of the much greater extent of water association. It should also be mentioned that the reported errors in Tables 2 and 3 represent a global analysis of error for the model fit. As has been shown previously with high certainties, the $C_3$ parameter is statistically significant and must be included in the fits or a large decrease in the Ni−O distance is obtained. With the inclusion of $C_3$ there is virtually no change in the Ni−O distance at higher temperatures.[12] Inclusion of $C_3$ in the fits did not affect the measured coordination numbers by >10%.

**Molecular Dynamic Simulation Results.** Figure 7 presents the Ni-edge *and* Br-edge $k^2$-weighted $\chi(k)$ plots for a 0.2 *m* NiBr$_2$ and 0.8 *m* NaBr solution at 425 °C and 0.62 g/cm$^3$ that were generated from the MD simulation (MD-XAFS) under
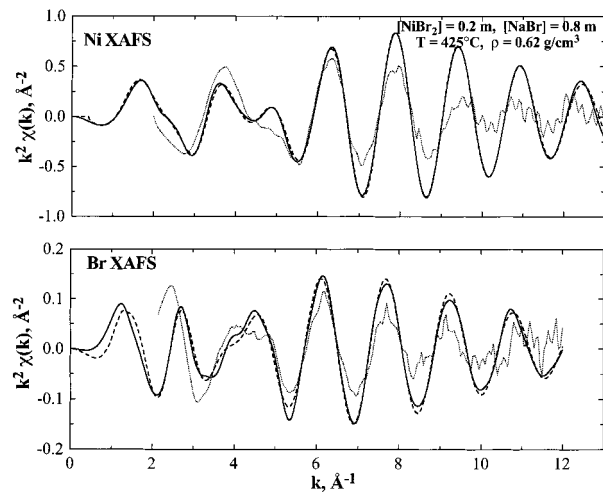


**Figure 7.** The *k*-weighted $\chi(k)$ plots for Ni$^{2+}$ and Br$^-$ XAFS from the MD simulations (MD-XAFS) corresponding to a system with 0.2 *m* NiBr$_2$ and 0.8 *m* NaBr solution at 425 °C and a density of 0.62 g/cm$^3$. For these simulations, the $N_{Br}$ was fixed at 3 for the duration of the simulation. The solid line shows the MD-XAFS and the dashed line shows the global model fit to both data sets using FEFF calculations and the parameters listed in Table 4. The dotted line corresponds to the experimentally determined XAFS. The fitted and simulated data have been scaled by the $S_0^2 = 0.85$ and $S_0^2 = 0.91$ for the Ni and Br XAFS, respectively.

conditions that match the experimental system. Also shown in Figure 7 is the model fit (dashed line) to the MD-XAFS spectra using the same global data reduction model that was used for the experimental system. The parameters from this fit are reported in Table 4. The MD-XAFS spectra were generated by a method previously described[10] that involves loading hundreds of equilibrated configurations from the MD simulation into the FEFF scattering code and then averaging the spectra to obtain a configurationally averaged XAFS spectra that positively captures the simulation structure.

For the MD simulation, the initial conditions were chosen so that the number of Br$^-$ in the first shell ($N_{Br}$) was equal to three. This value was chosen based on the experimental result. As has been previously described[12] for this MD model of aqueous NiBr$_2$, the structure of the solvation shell was remarkably stable at supercritical conditions on the time scale of the simulations. The simulation can be run for at least 50 ps without seeing any exchange of the bromine ions between the first shell and the rest of the solution, nor was any exchange seen when more than one simulation of the system was performed. The bromine ions that were placed on the Ni$^{2+}$ at the start would persist over the course of the simulation. Because of this, not much is known about the actual thermodynamic distribution of contact-ion pairs for the model at supercritical conditions. This information could be obtained from extensive free energy integration,[36] although this has not been done for this model. However, the *structural equilibration* within the first shell occurs *rapidly* even though the thermodynamic distribution of ion pairs was not determined. This rapid structural equilibration was determined from the fact that the nickel−oxygen and the first peak in the nickel−bromine radial distribution functions were the same when more than one run was performed on the system. This aspect allows one to realistically test the most probable structures of the experimental system. These spectra can be compared with the experimental spectra and used to test the degree of contact-ion pairing or to test the quality of the intermolecular potentials that are used in the simulation by how well they reproduce the first-shell structural details.

Ni$^{2+}$ Complex Structure Transition in Supercritical Water

*J. Phys. Chem. A, Vol. 103, No. 42, 1999* **8477**

**TABLE 4: Global Model Fit to *Both* Ni and Br XAFS from MD Simulations [The same data reduction method (FEFFIT) was applied to the MD-XAFS that was used to recover the experimental parameters given in Table 2. Results of XAFS analysis of first-shell Ni$^{2+}$ hydration, first-shell Br$^-$ hydration and for the Ni$^{2+}$/Br$_n$ ion pair under supercritical conditions. For the global fit, the relationship between the number of Br$^-$ about Ni$^{2+}$ ($N_{Br}$) and the number of Ni$^{2+}$ about Br$^-$ ($N_{Ni}$) is defined as $N_{Ni} = N_{Br}([Ni^{2+}]/[Br^-])$.]**

| Ni$^{2+}$/H$_2$O interaction | | | Ni$^{2+}$/Br$^-$ interaction | | | | Br$^-$/H$_2$O interaction | | | |
|---|---|---|---|---|---|---|---|---|---|---|
| $N_{H_2O}$ | $R$, Å | $\sigma^2 \times 10^3$, Å$^2$ | $N_{Br}$ | $R$, Å | $\sigma^2 \times 10^3$, Å$^2$ | $C_3 \times 10^4$ | $N_{H_2O}$ | $R$, Å | $\sigma^2 \times 10^3$, Å$^2$ | $R^a$ |
| | | | [NiBr$_2$] = 0.2 *m*, [NaBr] = 0.8 *m*, T = 425 °C, P = 410 bar, $\rho$ = 0.62 g/cm$^3$ | | | | | | | |
| 1.1 (0.2) | 2.151 (14) | 10.8 (3.1)$^b$ | 2.8 (0.1) | 2.430 (02) | 5.0 (0.2) | 5.1 (0.4) | 3.8 (1.0) | 3.657 (78) | 77.7 (15.5)$^c$ | 0.002 |

$^a$ Goodness of fit defined by a scaled sum of squares as described in FEFFIT.[27] $^b$ The fitted $C_3 \times 10^4$ is 21.0 (7.5) for the Ni−O inteactions. $^c$ The fitted $C_3 \times 10^4$ = 158.0 (93.0) for the Br−O inteactions.
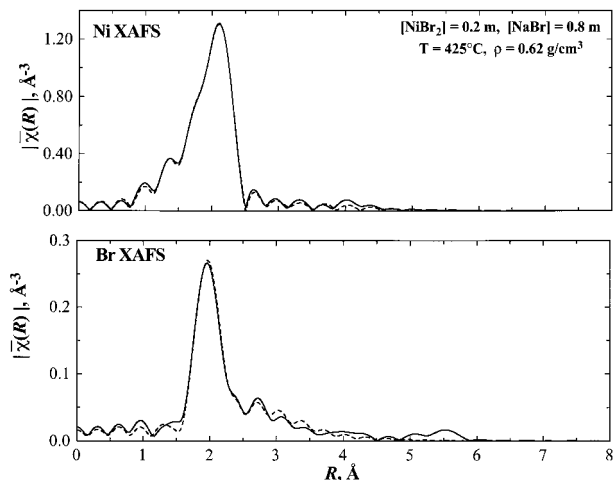


**Figure 8.** The $|\tilde{\chi}(R)|$ plot from the 0.2 *m* NiBr$_2$ and 0.8 *m* NaBr spectra shown in Figure 7 at 425 °C and 0.62 g/cm$^3$. For these simulations, the $N_{Br}$ was fixed at 3 for the duration of the simulation. The solid line shows the MD-XAFS results and the dashed line shows the global model fit to these MD results using FEFF calculations and the parameters listed in Table 4. The fitted and simulated data have been scaled by the $S_0^2$ = 0.85 and $S_0^2$ = 0.91 for the Ni and Br XAFS, respectively. The $|\tilde{\chi}(R)|$ plot is uncorrected for phase shifts whereas the corrected distances are reported in Table 2.

In Figure 7, we can clearly see that the simulation is capable of capturing the main features of the experimental spectra (dotted line). There are significant differences in the amplitudes of the oscillations both in the high *k* region from the Br or Ni XAFS contribution and in the low *k* region from the water contribution. This discrepancy is primarily due to a real difference in the experimental and MD $\sigma^2$ values, as is shown in the tabulated parameters in Tables 2 and 4. One explanation for the higher experimental Debye−Waller factor for the Ni$^{2+}$/Br$^-$ interaction is that it may contain contributions from some static disorder. This situation would occur if the Br$^-$ coordination about the Ni$^{2+}$ has slightly different ligand binding distances. This aspect would not be correctly captured in the MD simulations. These results indicate that further refinements of the intermolecular potentials is required before they can accurately simulate the behavior of ionic solutions at supercritical conditions.

Figure 8 presents the corresponding $\tilde{\chi}(R)$ plot from the transformed $\chi(k)$ data of the MD-XAFS given in Figure 7. The most significant feature of the $\tilde{\chi}(R)$ is the absence of a significant doublet that is associated with the two different distances of the nearest neighbors, Ni−O/Ni−Br (Ni XAFS) and Br−O/Br−Ni (Br XAFS). The primary reason for this absence is again that the $\sigma^2$ for the Ni−Br path is much too low relative to the experimental value ($\sigma^2 = 0.005$ Å$^2$ for the MD-XAFS versus $\sigma^2 = 0.012$ Å$^2$ for the experiment). A second reason is that $\sigma^2$ for the Ni−O path is much too high relative to the experimental value ($\sigma^2 = 0.012$ Å$^2$ for the MD-XAFS versus $\sigma^2 = 0.003$ Å$^2$

for the experiment). In the Fourier-transformed spectra, the large amplitude of the Ni−Br contribution (in both $\tilde{\chi}(R)$ plots) dominates the much smaller water peaks. Even with this one dominant term, the data reduction method is successful at recovering the number of water molecules about the Ni$^{2+}$ and the Br$^-$ that correspond well with the values directly calculated from the radial distribution function (Figure 9) from the MD simulation. This good correspondence is shown by comparing the values in Tables 4 and 5. Other than the differences in $\sigma^2$, the simulation does a reasonable job of correctly predicting the experimental coordination numbers and distances. To obtain the parameters in Table 5, the first peak in the radial distribution function is fit to the function

$$G(R) = A(1 + a(R - R_0)^3 + b(R - R_0)^4)e^{-(R - R_0)^2/2\sigma^2} \quad (5)$$

where $A$, $a$, $b$, and $\sigma$ are adjustable parameters. The third cumulant $C_3$ can be obtained by integrating the third moment of this function, and the Debye−Waller factor is the width of the Gaussian, $\sigma$. The coordination numbers are obtained directly from the $G_{ij}(r)$ by integrating them out to the first minima. These numbers can then be compared with the parameters obtained from fitting the MD-XAFS spectra to eq 1, as well as with the parameters obtained by fitting the experimental XAFS spectra.

Figure 9 presents the various radial pair distribution functions, $G_{ij}(r)$, for the NiBr$_2$/NaBr system at 425 °C. The first peaks in both $G_{NiBr}(r)$ and $G_{NiO}(r)$ are very narrow, primarily a result of the small radius and divalent charge of the Ni$^{2+}$. In contrast, the $G_{BrO}(r)$ is very broad and diffuse, corresponding to the much larger, monovalent anion and the orientation of the water molecules in this case where the proton sits between the Br$^-$ and the O. Also shown in Figure 9 is the $G_{BrBr}(r)$. This peak is due to Br−Br associations from the Br ions in the first-shell about the Ni$^{2+}$. Compared with $G_{NiBr}(r)$, we find significant broadening in the $G_{BrBr}(r)$ either from increased dynamic or static disorder of these Br ions on the surface of the Ni$^{2+}$. From all of these different $G_{ij}(r)$ values we can directly determine coordination numbers, distances, and an estimated $\sigma^2$ by fitting the first peak in the $G_{ij}(r)$ to the modified Gaussian function in eq 5. These values are reported in Table 5.

Figure 10 presents two additional $G_{ij}(r)$ values. The first is for the $G_{BrNa}(r)$, that primarily corresponds to the ion-pairs species that are formed about those Br ions that are not associating with the nickel. The first peak in the $G_{BrNa}(r)$ at a distance of 2.95 Å represents this Na−Br contact-ion pair distance. The second function in Figure 10 is for $G_{NiNa}(r)$, showing the distribution of Na$^+$ about the Ni$^{2+}$. In the simulation, the tribromo nickel complex, NiBr$_3^{-1}$, has a net negative charge. At this fluid density ($\rho$ = 0.62 g/cm$^3$), the relatively strong electrostatic forces drive all complexes toward associations that are neutraly charged. Hence, the simulation shows the relative position of the Na$^+$ ions that are associating with the tribromo nickel complex. The distance of the first peak

**TABLE 5: Structural Parameters Obtained Directly from the Molecular Dynamics Pair Distribution Functions, $G_{ij}(r)$ (Figure 7) (The $G_{ij}(r)$'s were derived from the same set of configurations that were used to generate the XAFS spectra and the parameters reported in Table 4. Results include the analysis of first-shell $Ni^{2+}$ hydration, first-shell $Br^-$ hydration and for the $Ni^{2+}/Br_n$ ion pair under supercritical conditions.)**

| $Ni^{2+}/H_2O$ interaction | | | $Ni^{2+}/Br^-$ interaction | | | | $Br^-/H_2O$ interaction | | |
|---|---|---|---|---|---|---|---|---|---|
| $N_{H_2O}$ | $R$, Å | $\sigma^2 \times 10^3$, Å$^2$ | $N_{Br}$ | $R$, Å | $\sigma^2 \times 10^3$, Å$^2$ | $C_3 \times 10^4$ | $N_{H_2O}$ | $R$, Å | $\sigma^2 \times 10^3$, Å$^2$ |
| | | | [NiBr$_2$] = 0.2 $m$, [NaBr] = 0.8 $m$, $T$ = 425 °C, $P$ = 410 bar, $\rho$ = 0.62 g/cm$^3$ | | | | | | |
| 1.1[a] | 2.071 | 6.9[b,c] | 3.0 | 2.388 | 5.2[b] | 1.6[b] | 4.1[d] | 3.429 | 63.3[b,e] |

[a] From the integrated $G_{NiO}(r)$ out to 2.8 Å. [b] Calculated from a modified Gaussian form fitted to the first peak in $G_{ij}(r)$ as described in eq 5. [c] The calculated $C_3 \times 10^4$ = 4.1 for the Ni–O interactions. [d] From the integrated $G_{BrO}(r)$ out to 3.94 Å. [e] The calculated $C_3 \times 10^4$ = 210 for the Br–O interactions.
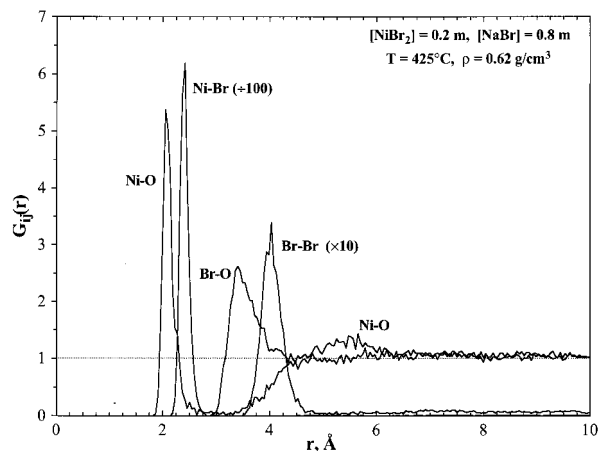


**Figure 9.** Pair distribution functions, $G_{ij}(r)$, from the MD simulation for the 0.2 $m$ NiBr$_2$ and 0.8 $m$ NaBr solution at 425 °C and a density of 0.62 g/cm$^3$. For these simulations the $N_{Br}$ was fixed at 3 for the duration of the simulation. The $G_{ij}(r)$ values are derived from the same set of configurations that were used to generate the XAFS spectra in Figure 7.
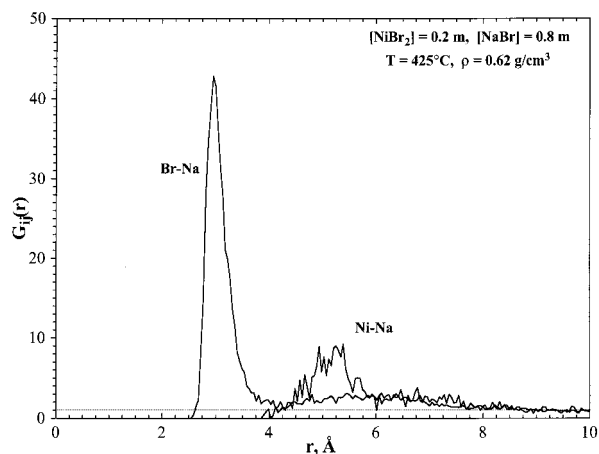


**Figure 10.** Pair distribution functions, $G_{ij}(r)$, from the MD simulation for the 0.2 $m$ NiBr$_2$ and 0.8 $m$ NaBr solution at 425 °C and a density of 0.62 g/cm$^3$. For these simulations the $N_{Br}$ was fixed at 3 for the duration of the simulation. The $G_{ij}(r)$ values are derived from the same set of configurations that were used to generate the XAFS spectra in Figure 7.
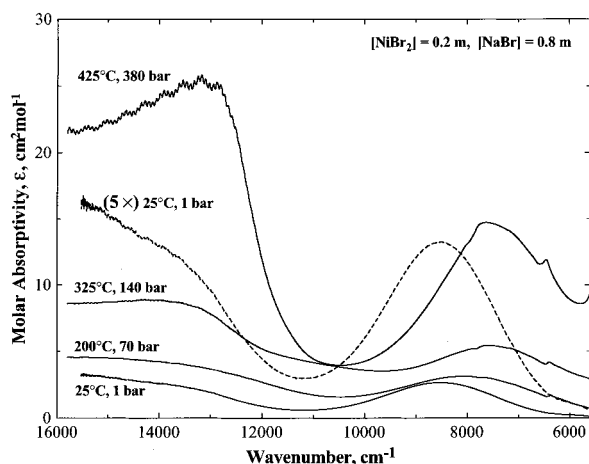
in $G_{NiNa}(r)$ at $\sim$5.2 Å corresponds to Na$^+$ that is near the *exterior* of the tribromo nickel complex at a distance corresponding to a direct Br$^-$ contact. Upon integrating the first peak in the $G_{NiNa}(r)$ function out to a distance of 6 Å, we find a total of $\sim$0.7 Na$^+$ ions in this shell, although this is only an approximate number because this aspect of the simulation may not have completely converged. Nevertheless, the simulation does tend toward a neutraly charged complex. It is significant that even for this large multiatomic complex, the charge-neutral species are strongly favored.

The simulation results fortify all aspects of the experimental data reduction method. There are several important conclusions that can be drawn from this exercise. Foremost, as has previously been demonstrated for other systems,[10,12,15] the data reduction technique (FEFFIT) that is used to obtain the first-shell parameters generates values that are in excellent agreement with the values determined directly from the $G_{ij}(r)$ values (Table 4 versus Table 5). Second, if we compare the MD-XAFS parameters (Table 4) with the experimental parameters (Table 2), we find good qualitative agreement for the various first-shell parameters, again with the single qualification that $N_{Br}$ is artificially set at 3 in the simulation. Even though we find a good "first-order" agreement between the simulation and the experiment, there are obvious defects in the intermolecular potentials that were chosen for these simulations. In particular, the $\sigma^2$ values for Ni–O, Ni–Br, and Br–O that are directly related to the width of the first peak in the $G_{ij}(r)$ values are not accurately reproduced in the simulation. To improve these parameters, some refinements of the $\epsilon_i$ in the Lennard–Jones potential may be required or ultimately a more complex intermolecular potential function may be needed. Thus it is demonstrated that the experimental XAFS may be used to test and refine the intermolecular potentials. This usefulness is especially true in light of the high level of accuracy of the current XAFS scattering codes (e.g.; FEFF). Finally, it is also significant that the simulation produces a tetrahedral species (tribromo monoaqua nickel) for this case with $N_{Br}$ = 3, without including any information about molecular orbital structure for this transition metal. This result suggests that the structure of these clusters is dominated by steric and electrostatic interactions.

**The Ni Preedge and the Near-Infrared Spectra.** Figures 5 and 6 present a temperature series of the Ni preedge spectra for the 0.2 $m$ NiBr$_2$ and the 0.2 $m$ NiBr$_2$/0.8 $m$ NaBr solutions, respectively. Figure 11 presents the NIR spectra for the 0.2 $m$ NiBr$_2$/0.8 $m$ NaBr solution. Whereas the preedge spectra contain information about electronic transitions between atomic orbitals, the NIR absorption bands arise from electronic transitions between molecular orbitals of the Ni$^{2+}$ complexes. Both are governed by different sets of symmetry selection rules and together they provide evidence of the types of the Ni$^{2+}$ coordination that occur at high temperatures.

In Figures 5 and 6, the two Ni preedge peaks are assigned to $1s \rightarrow 3d$ and to $1s \rightarrow 4p$ transitions.[37] The spectra shown in Figures 5 and 6 were acquired with two different X-ray optical setups. The earlier series, for the 0.2 $m$ NiBr$_2$, was acquired at significantly lower energy (eV) resolution (>2 eV) than the spectra acquired for the solutions containing NaBr (<1 eV). Thus, in Figure 5, the $1s \rightarrow 4p$ transition is not clearly resolved. However, upon examination of the spectra in Figure 6, which has much higher energy resolution, one can clearly ascribe the increased intensity in the spectral region from 8337 to 8342 eV to the $1s \rightarrow 4p$ transition. The $1s \rightarrow 3d$ transition for this

Ni$^{2+}$ Complex Structure Transition in Supercritical Water

*J. Phys. Chem. A, Vol. 103, No. 42, 1999* **8479**



**Figure 11.** The NIR spectra of Ni$^{2+}$ in a D$_2$O solution. The apparent molar absorptivities are reported. The absorbances are corrected for differences in the concentration, path lengths, and solution molecular densities, but no correction is made for the small changes in beam transmission with density. Glitches at 7500 and 6500 cm$^{-1}$ are due to incomplete subtraction of the pure D$_2$O background spectra that contains sharp, but weak overtone vibrational bands in this region.

0.2 $m$ NiBr$_2$ solution was previously reported[12] and there was little or no change in the measured intensity. However, the lower energy resolution of this spectra would not allow for detection of small changes (25%), if they exist.

In Figure 6a, the entire preedge region and part of the XANES region is displayed out to ~15 eV above the absorption edge with high energy resolution. In Figure 6b the vertical axis has been expanded to show the region of the $1s \rightarrow 3d$ transition. Figure 6c shows the derivative spectra to better illustrate the region about the $1s \rightarrow 4p$ transition. The intensity of both of these bands increases significantly at higher temperatures. The implications of these changes will be described in detail in the following sections.

In Figures 6a and 6c, it is also important to note the position and behavior of the Ni absorption edge. For nickel, 8333 eV is the defined absorption edge for Ni$^0$ (metal) based on the conduction band of the $1s \rightarrow 3d$ transition. As one would expect for the Ni$^{2+}$ solutions, the absorption edge is now at an energy just slightly above the $1s \rightarrow 4p$ transition at ~8342 eV. This increase in the edge energy is primarily due to an absence of the Fermi conduction band for the nickel in solution; however, it is also due to a change in the formal oxidation state of nickel and to the partial delocalization of the charge on the formation of the molecular orbitals. In Figure 6c, we see strong evidence of the constancy of $E_0$ ($\pm0.5$ eV) in the region near 8342 eV, showing the overlap of the slopes in this region (just above the $1s \rightarrow 4p$ transition). Thus we conclude that there is little or no delocalization of the charge on the Ni$^{2+}$ ion on changing the coordination at higher temperatures.

In Figure 6a, the large decrease in the intensity with increasing temperature in the region beyond the absorption edge (8352 eV) is believed to be due to the loss of the MS paths (O–Ni–O) from the octahedrally coordinated species Ni(H$_2$O)$_6$$^{2+}$. This decrease in intensity is primarily due to the change in the coordination structure about Ni$^{2+}$ but may also be due in part to the greater thermal disorder of the octahedral species and the large susceptibility of the amplitude of MS paths to this disorder. A third explanation for the large decrease in intensity of this region is that there may be some diffuse contribution, at very low $k$, from second-shell hydration about Ni$^{2+}$ whose structure is also destroyed under higher temperature

conditions. In general, it is important to emphasize that we are measuring only the first-shell structure from the XAFS region and that in many cases, where there will be a weak, second-hydration shell, this structural feature is not assessable by XAFS because of the high degree of disorder and longer distance associated with this feature.

In Figure 11, the NIR spectra from 6500 to 16 000 cm$^{-1}$ is presented for a series of temperatures for the solution containing 0.2 $m$ NiBr$_2$ and 0.8 $m$ NaBr. These spectra were acquired in D$_2$O solutions to avoid interfering H$_2$O solvent bands located at ~7500 cm$^{-1}$. Further, the vertical axis represents the apparent molar extinction coefficient for which corrections have been made for the changes in the solution density, the cell path lengths, and NiBr$_2$ concentrations. However, no changes have been made to account for the differences in the transmission that occur with the changing density, although this is expected to be a relatively small correction to the reported extinction coefficients (<10%). The small residual spectral features at 6500 and 7800 cm$^{-1}$ of the high-temperature spectra are due to incomplete subtraction of two small D$_2$O overtone bands whose band shape is weakly affected by the presence of the salts. Upon heating the solution from ambient to 425 °C, we observe a transition of the 8500 cm$^{-1}$ band to a much more intense band centered at 7000 cm$^{-1}$. Also, the mode located at about ~13 800 cm$^{-1}$ is replaced by a very strong band at 13 200 cm$^{-1}$. The bands at 8500 and at ~13 800 cm$^{-1}$ for the low-temperature spectra are assigned to the $^3A_{2g} \rightarrow {}^3T_{2g}$ and $^3A_{2g} \rightarrow {}^3T_{1g}$ transitions of the octahedral structure.[38] At higher temperatures, the new bands at 7000 and 13 200 cm$^{-1}$ are assigned to the $^3T_1 \rightarrow {}^3A_2$ and $^3T_1 \rightarrow {}^3T_1(P)$ transitions of the tetrahedral species.[38] These spectral changes are consistent with a change in the degree of coordination about the Ni$^{2+}$ ions.

## Discussion

In the following sections, we first show that based on the collective evidence of four independent measurements, Ni$^{2+}$ undergoes a coordination change from a 6-coordinate species at room temperature to a 4-coordinate species at 425 °C. We then use the various spectroscopic results (Ni XAFS, Br XAFS, Ni preedge spectra, and NIR spectra) to identify the symmetry of the 4-fold coordination structures at this temperature. Finally, we discuss the significance of the experimental data with respect to improving the ion-pair potentials in the MD simulations.

**XAFS Measurements of Coordination Changes.** Figure 12 shows the changes in local coordination structure about Ni$^{2+}$ as a function of temperature for the 0.2 $m$ NiBr$_2$/0.8 $m$ NaBr solution (from the values reported in Table 3). Also shown are the values for the solution without added NaBr that were obtained from an earlier work.[12] For these two different salt concentrations (and at pressures <1 kbar), there are large changes in the coordination structure in the region around the critical point of water ($T_c$ = 375 °C). In this region, there is some reduction in the density of the solution but there is a large decrease in the dielectric constant due to breaking of the water hydrogen-bonding network.[1] The measured solution densities reported in Table 3 show that for all conditions >325 °C, the fluid density is ~0.5 g/cm$^3$. The coincidence of the rapid change in the solvent dielectric constant with the large changes in the coordination structure implies that the formation of the bromo nickel species is driven mostly by electrostatic factors and not solely due to simple temperature or density effects. When the total Br$^-$ concentration is increased with the addition of the NaBr, there is a large increase in those NiBr$_n$$^{(2 - n)+}$ species with greater Br$^-$ coordination. However, even at the highest
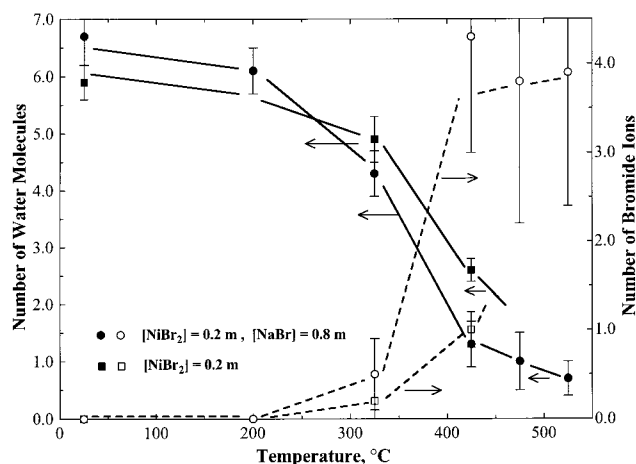
**Figure 12.** Change in the first solvation shell structure about $Ni^{2+}$ with increasing temperature. The number of water molecules decreases and the number of bromide ions increases in the temperature region above the critical point of water. Two different concentrations are represented, corresponding to the data from Table 3 for the systems with NaBr and to the data reported in ref 12 for the systems with only $NiBr_2$. The data are derived from Ni XAFS measurements. The lines are included to guide the eye.

temperatures, there is still ∼1 water molecule about the $Ni^{2+}$. Further, there is unequivocal evidence of first-shell water association about $Ni^{2+}$ even at 525 °C from the low-$k$ oscillations in the XAFS spectra (not shown), although the amount of water may slightly decrease from 425 to 525 °C (Table 3). For this system, in which there is a high concentration of $Br^-$, no evidence of any Ni−Br association is found for temperatures ≤200 °C.

As discussed in the *Results*, the global structural parameters summarized in Table 2 produce excellent agreement with both the Ni and Br XAFS data. Hence, there is high confidence that the structure that exists at 425 °C in both solutions is a 4-coordinate $NiBr_n(H_2O)_{4-n}$ species or, more precisely, one with an average of 3.6 nearest neighbors (2.4 O, 1.2 Br) and 4.3 nearest neighbors (1.0 O, 3.3 Br) for the systems without and with added NaBr, respectively. Simply on the basis of the fact that the average coordination number is so close to 4, there can be little or no 6-coordinate species in equilibrium with the 4-coordinate species or the averages would be significantly higher. There is other qualitative evidence, that for temperatures of ≥425 °C, only the 4-coordinate species exist. This evidence can be found in the preedge spectra given in Figure 6. The $1s \rightarrow 3d$ and $1s \rightarrow 4p$ transitions both increase to a nearly constant value at 425 °C and above. The XANES, multiple-scattering peak at ∼8352 eV decreases to a constant value as the temperature is increased to 425 °C. Another $Ni(H_2O)_6^{2+}$ multiple-scattering peak at 8365 eV (shown in Figure 6) also disappears into the single-scattering baseline at temperatures >325 °C. This collective evidence indicates that most likely a *single*, 4-coordinate $Ni^{2+}$ species predominates at conditions >425 °C; that is, the tribromo monoaqua species for the system with NaBr and the monobromo triaqua species for the system without added NaBr.

For the systems measured with both Ni and Br XAFS, the jointly shared parameters in the model fits are those related to the Ni−Br structure whose contribution to the $\chi(k)$ plots in Figures 1 and 2 is predominately above $k = 5$ Å$^{-1}$. The usable XAFS range extends out to about $k = 12$ Å$^{-1}$. Thus, there is a high degree of confidence in the measured distance, coordination number, Debye−Waller factor, and the third cumulant (anharmonicity term, $C_3$) that are reported in Table 2 for the Ni−Br
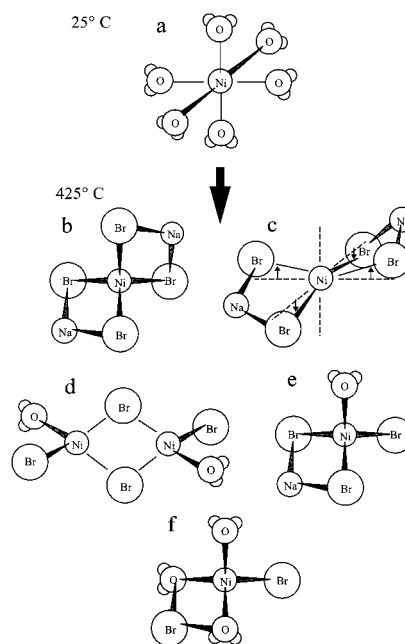


**Figure 13.** $Ni^{2+}$ structural transition from 6- to 4-coordinate at high temperatures. The waters of hydration about the $Br^-$ are not shown for clarity. Species b−f represent five possible, electrostatically neutral, ion-pair species including (b) tetrahedral (tetrabromo), (c) distorted square planar, (d) tetrahedral Ni dimer species, (e) tetrahedral (tribromo monoaqua), and (f) tetrahedral (monobromo triaqua) with a solvent-separated bromide ion pair.

coordination. It is important to note that the third cumulant can affect the measured Ni−Br distance by as much as 0.1 Å, but because we have a reasonable measurement of the third cumulant we can place high confidence in the measured distance for these two systems of 2.41 Å. This distance is 0.14 Å less than our measurement of the Ni−Br distance in the solid $NiBr_2$ salt.

**Symmetry of Possible High-Temperature Ni−Br$_n$ Structures.** We have established that the structure about $Ni^{2+}$ changes from 6- to 4-coordinate upon increasing the temperature from 25 to 425 °C. Now we discuss which of various possible 4-coordinate species are most likely to be present. Figure 13 shows several possible high-temperature structures of the Ni−Br$_n$ contact-ion pairing. The accepted structure at room temperature for all salt concentrations is the pure octahedral geometry with 6-coordinated water molecules depicted in Figure 13a. At high temperatures, there are a multitude of different possible structures, including the pure tetrahedral, tetrabromo nickel complex (Figure 13b), a distorted square planar species (Figure 13c), a Ni dimer species (Figure 13d), a 4-coordinate tribromo monoaqua complex (Figure 13e), and a 4-coordinate monobromo triaqua complex (Figure 13f).

At high temperatures, the decrease in the dielectric constant of water strongly favors the formation of neutral species. Thus, Figure 13 not only depicts the $Ni^{2+}$ associations with $Br^-$ but also the corresponding association of $Br^-$ with the $Na^+$ to ensure the neutral complex. Formation of $Ni^{2+}$ species with $Br^-$ coordination of >2 suggests that these species must contain multiple cations, either $Ni^{2+}$ or $Na^+$, to form neutral species (structures in Figures 13b−e). For systems containing only $NiBr_2$, the highest association is probably the $NiBr_2(H_2O)_2$ species. Further, simply based on the packing restrictions of the large-size $Br^-$ ion about the relatively small $Ni^{2+}$ ion, the distorted square planar or tetrahedral structure should be strongly preferred over the pure square planar structure.[4,39] Finally for all of the tetrahedral structures represented in Figures 13b−f

excepting the NiBr$_4$ species, a pure tetrahedral species cannot be expected. Thus, the structures in Figures 13e and 13f are necessarily slightly distorted.

**Symmetry Details from the XAFS Spectra.** Based on the results that are summarized in Table 2, the XAFS data strongly support the existence of the monobromo triaqua and tribromo monoaqua nickel complexes at 425 °C for the NiBr$_2$ and the NiBr$_2$/NaBr solutions, respectively. The failure to observe the neutral-charged, dibromo diaqua nickel species for the 425 °C solution might be because of the existence of a solvent-separated ion pair (Figure 13f).

All of the first-shell atoms (shown in Figures 13a−f) about the central absorbing atom contribute to measured XAFS scattering. Thus, it is possible to further exploit the XAFS data and test for the existence of some of the hypothetical structures in Figure 13 based on whether certain scattering contributions are, or are not observed. The latest XAFS scattering codes (e.g.; FEFF7) provide a very high level of performance and the capability to test potential scattering paths against the measured XAFS spectra. For instance, for the dimer (Figure 13d) and higher polymer species, one could reasonably expect to see significant Ni−Ni scattering paths. However, the similarity in the Ni−Ni distance (∼2.78 Å) and the Ni−Br distance (2.41 Å) combined with the fact that the $\sigma^2$ for the Ni−Ni path is probably >0.012 Å$^2$ means that this scattering path would be difficult to detect. A similar argument is valid for failure to find significant Br−Na scattering contributions. Here, the interference is with the oxygens ($Z = 8$ versus 11 for Na) on the water molecules and again the similarity in the atomic distance for these two species. Thus, structural simulations using FEFF7 tell us that for this particular system it is not possible to experimentally observe Ni−Ni or Br−Na structures with XAFS.

More conclusions are possible with this approach. For the system containing added NaBr salt, there are on average ∼3 Br$^-$ about the Ni$^{2+}$. Thus, another expected scattering contribution might be the Br−Br single-scattering paths. For the tetrahedral structure, the Br−Br distance would be ∼3.94 Å. Although this distance is quite large, modeling this contribution using FEFF indicates that this scattering contribution would be observed experimentally if the Debye−Waller factor, $\sigma^2$, was similar to $\sigma^2 = 0.012$ Å$^2$ for the Br−Ni path. Failure to experimentally observe this scattering path leads to the conclusion that even though the Br$^-$ are tightly bound to the Ni$^{2+}$, the tangential disorder ($\sigma^2 > 0.012$ Å$^2$) of the Br$^-$ on the surface of the Ni$^{2+}$ is significantly larger than the radial disorder. This observation supports the conclusion that the high-temperature species is not a rigid tetrahedral structure. The MD simulations confirm the expectation of higher Br−Br disorder. In Figure 9 we observe that the first peak in $G_{BrBr}(r)$ is more than twice the width of $G_{NiBr}(r)$, and thus these Br−Br scattering paths would not be observed by XAFS.

Testing scattering paths of different structural models with FEFF allows us to draw conclusion about the existence of several different 4-coordinate structures. However, from the XAFS alone we cannot conclusively exclude any of the 4-coordinated species (the distorted square planar, dimer, or distorted tetrahedral structures) in Figure 13.

In the following sections we can further refine our conclusions about the high-temperature Ni$^{2+}$ structure from an analysis of the preedge and NIR spectra.

**Symmetry Details from the X-ray Absorption Preedge Spectra.** Waychunas and Brown[37] have provided a detailed description of the bound-state transitions and the effects of symmetry changes on the allowed electronic transitions for metal

ions in various minerals that are also applicable to the present system. Thus the two Ni preedge peaks shown in Figure 6 are assigned to $1s \rightarrow 3d$ and to $1s \rightarrow 4p$ transitions. For the octahedral-coordinated, hexa-aqua nickel at room temperature, the $1s \rightarrow 3d$ transition is not allowed; however, through either a slight amount of thermal disorder, $3d \rightarrow np$ mixing, or quadrapolar coupling, a slight intensity is observed.

A large number of 4-coordinate nickel(II) complexes have square planar geometry.[39] We conclude for the following reasons that the 4-coordinate species is not a pure square planar geometry because only the $1s \rightarrow 4p$ transition would be allowed in this case and not the $1s \rightarrow 3d$ transition. In contrast we also observed a significant *increase* in the intensity of the $1s \rightarrow 3d$ transition. The intensity of the $1s \rightarrow 3d$ transition is (after baseline correction and edge-height normalization) ∼2.5 times higher at temperatures >425 °C. This increase is similar to that expected for a transition from an octahedral to a tetrahedral structure where an increase in the intensity of a factor of ∼3 has been observed in nickel silicate glass.[40,41] However, this comparison is not exact because the first-shell structure for these aqueous systems contains both Br$^-$ and H$_2$O in contrast to the case for glasses in which the first shell contains only O, which may also affect the intensity of this band. We also cannot positively exclude such species as a distorted 5-coordinate Ni$^{2+}$ from the behavior of this transition.

The $1s \rightarrow 4p$ transition is allowed for octahedral coordination and for any 4- or 5-coordinated nickel species regardless of the symmetry, although the transition probabilities vary between these species. The large increase in the intensity of this band for the Ni$^{2+}$ systems (See Figures 5b and 6c) appears to occur with addition of Br$^-$ into the first-shell structure. A similar intensification of this band was observed for the two standard powder materials Ni(OH)$_2$ and NiBr$_2$. These reference compounds both have pure octahedral coordination, but the intensity of the $1s \rightarrow 4p$ transition at ∼8342 eV is 2−3 times higher for the Br-coordinated Ni$^{2+}$ than for the O-coordinated species. Thus, the intensity increase of this band shown in Figures 5 and 6 is further evidence of the formation of the Ni$^{2+}$/Br$^-$ ion-pair species at elevated temperatures.

The preedge spectra are not inconsistent with the conclusions from the XAFS spectra and the MD analysis that when one or more Br$^-$ associates with a Ni$^{2+}$ the coordination structure changes to a distorted tetrahedron. Whether this change occurs in the absence of Br$^-$ in the first-coordination shell when only water associates at higher temperature cannot be determined with the present data because at these concentrations a preponderance of ion pairs forms at temperatures >325 °C.

**Symmetry Details from the Near-Infrared Spectra.** Crystal field theory can be used to successfully describe the low-energy electronic transitions for these Ni$^{2+}$ complexes. For the room-temperature Ni(H$_2$O)$_6$$^{2+}$ species, the bands at 8500 and at ∼13 800 cm$^{-1}$ are assigned to the $^3A_{2g} \rightarrow {}^3T_{2g}$ and $^3A_{2g} \rightarrow {}^3T_{1g}$ transitions of the octahedral structure, respectively.[38] At high temperature, the new bands at 7000 and 13 200 cm$^{-1}$ are assigned to $^3T_1 \rightarrow {}^3A_2$ and $^3T_1 \rightarrow {}^3T_1(P)$ transitions of the tetrahedral species, respectively.[38] The relative intensity of the 13 200 cm$^{-1}$ band is lower than that of the tetrabromo species,[38] NiBr$_4$$^{-2}$, and hence the results support the existence of lower Br-coordinated species and/or a distorted tetrahedral structure. For a distorted tetrahedra, varying degrees of Br$^-$ adduction will alter the band intensity and may also alter the band position by as much as several 100 wavenumbers. Further, without more complete crystal field spectra, including the visible range, it is

not possible to exclude the possibility of 5-coordinate species using the NIR spectra alone.

There is a very large increase in the molar extinction coefficient for all tetrahedral species. The molar extinction coefficient can be 10 to 100 times larger than for the octahedral complex. This range makes quantitative analysis of the concentration of the different states difficult. From these spectra we can only state that there is an appreciable amount of the tetrahedral species and that the octahedral species is greatly reduced. It is interesting to note that in an early UV–vis study by Lüdemann et al.[7] of the crystal field spectra of a $NiCl_2$ solution containing NaCl at temperatures up to 500 °C, one of the proposed structures was a trichloro monoaquo nickel complex. The transition to this 4-coordinate species is supported by our NIR measurements for the $NiBr_2$ system. Lüdemann et al.[8] also reported visible spectra for the $NiBr_2$ at higher temperatures. For the highest reported temperature of 300 °C, the start of the transition to a different coordination species was observed, but no convincing evidence of the tetrahedral structure was reported because the temperatures were not quite high enough to observe appreciable amounts of the tetrahedral species.

It is apparent that from a more thorough treatment of the X-ray preedge intensities and transitions *with* the NIR band intensities and transitions that the complete equilibrium speciation may be obtained in the transition temperature range 325–425 °C with these methods. However, a quantitative treatment of the preedge features is currently not available. Thus, we are primarily limited here to conclusions regarding the structure of the tetrahedral species that exist for temperatures ≥425 °C.

## Conclusions

The first-shell coordination structure about $Ni^{2+}$ at elevated temperatures has been determined from a global model fit to both Ni and Br XAFS measurements. The structure determined from this method is in agreement with the X-ray preedge peak and with NIR measurements of the same system. All the techniques show that large structural changes occur between 325 and 425 °C. However, at somewhat higher temperatures up to 525 °C (and densities of ∼0.5 g/cm³), almost no additional change in the structure was observed.

For temperatures ≥425 °C, the predominant species is a distorted tetrahedral $Ni^{2+}$ complex with varying degrees of $Br^-$ adduction that is primarily controlled by the overall $Ni^{2+}$ and $Br^-$ concentrations but may also be affected by temperature. For the system containing only the 0.2 *m* $NiBr_2$ salt, the most likely species at 425 °C is the monobromo triaqua nickel complex. For the system that has a much higher $Br^-$ concentration from addition of the 0.8 *m* NaBr salt, the most likely species is the tribromo monoaqua nickel complex. Even at 525 °C this system still has ∼1 water molecule in the first coordination shell.

The MD simulations were used to test the methods of XAFS data reduction and to further explore the nature of the first-shell structure directly from the $G_{ij}(r)$ values. It is clear that the presently available intermolecular potentials are not suitable to quantitatively reproduce the high-temperature structure, in particular with regard to the Debye–Waller factor. However, they appear to do a good job of reproducing the qualitative behavior of these systems. The experimental XAFS may be used to improve these potentials as well as to further our understanding of the types of associations in these systems.

## References and Notes

(1) Hoffmann, M. M.; Conradi, M. S. *J. Am. Chem. Soc.* **1997**, *119*, 9, 3811–3817.

(2) Chialvo, A. A.; Cummings, P. T.; Simonson, J. M.; Mesmer, R. E. *J. Mol. Liq.* **1997**, *73, 74*, 361–372.

(3) Oelkers, E. H.; Helgeson, H. C. *Science* **1993**, *261*, 888–891.

(4) Angell, C. A.; Gruen, D. M. *J. Am. Chem. Soc.* **1966**, *88*, 5192–5198.

(5) Susak, N. J.; Crerar, D. A. *Geochim. Cosmochim. Acta* **1985**, *49*, 555–564.

(6) Spohn, P. D.; Brill, T. B. *J. Phys. Chem.* **1989**, *93*, 6224–6231.

(7) Lüdemann, H. D.; Franck, E. U. *Ber. Bunsen-Ges. Phys. Chem.* **1968**, *72*, 514–523.

(8) Lüdemann, H. D.; Franck, E. U. *Ber. Bunsen-Ges. Phys. Chem.* **1967**, *71*, 455–460.

(9) Pfund, D. M.; Darab, J. G.; Fulton, J. L.; Ma, Y. *J. Phys. Chem.* **1994**, *98*, 13102–13107.

(10) Palmer, B. J.; Pfund, D. M.; Fulton, J. L. *J. Phys. Chem.* **1996**, *100*, 13393–13398.

(11) Fulton, J. L.; Pfund, D. M.; Wallen, S. L.; Newville, M.; Stern, E. A.; Ma, Y. *J. Chem. Phys.* **1996**, *105*, 2161–2166.

(12) Wallen, S. L.; Palmer, B. J.; Fulton, J. L. *J. Chem. Phys.* **1998**, *108*, 4039–4046.

(13) Seward, T. M.; Henderson, C. M. B.; Charnock, J. M.; Dobson, B. R. *Geochim. Cosmochim. Acta* **1996**, *60*, 2273–2282.

(14) Ragnarsdottir, K. V.; Oelkers, E. H.; Sherman, D. M.; Collins, C. R. *Chem. Geol.* **1998**, *151*, 29–39.

(15) Wallen, S. L.; Palmer, B. J.; Pfund, D. M.; Fulton, J. L.; Newville, M.; Ma, Y.; Stern, E. A. *J. Phys. Chem. A* **1997**, *101*, 9632–9640.

(16) Hoffmann, M. M.; Darab, J. G.; Heald, S. M.; Yonker, C. R.; Fulton, J. L. *Chem. Geol.* In press.

(17) Baes, C. F.; Mesmer, R. E. *The Hydrolysis of Cations*; Krieger: Malabar, FL, 1976.

(18) Teo, B. K. *EXAFS: Basic Principles and Data Analysis*; Springer-Verlag: New York, 1986.

(19) Stern, E. A.; Heald, S. In *Handbook of Synchrotron Radiation*; Eastman, D. E.; Farge, Y.; Koch, E. E., Eds.; North-Holland: Amsterdam, 1983.

(20) *X-ray Absorption: Principles, Applications, Techniques of EXAFS, SEXAFS and XANES*; Koningsberger, D. C.; Prins, R., Eds.; John Wiley & Sons: New York, 1988.

(21) Newville, M.; Livins, P.; Yacoby, Y.; Rehr, J. J.; Stern, E. A. *Phys. Rev. B* **1993**, *47*, 14126–14131.

(22) Zabinsky, S. I.; Rehr, J. J.; Ankudinov, A.; Albers, R. C.; Eller, M. J. *Phys. Rev. B.* **1995**, *52*, 2995–3009.

(23) O'Day, P. A.; Rehr, J. J.; Zabinsky, S. I.; Brown, G. E., Jr. *J. Am. Chem. Soc.* **1994**, *116*, 2938–2949.

(24) Mustre de Leon, J.; Rehr, J. J.; Zabinsky, S. I. *Phys. Rev. B* **1991**, *44*, 4146–4156.

(25) Rehr, J. J.; Mustre de Leon, J.; Zabinsky, S. I.; Albers, R. C. *J. Am. Chem. Soc.* **1991**, *113*, 5135–5140.

(26) Frenkel, A. I.; Stern, E. A.; Qian, M.; Newville, M. *Phys. Rev. B* **1993**, *48*, 12449–12458.

(27) Newville, M.; Ravel, R.; Haskel, D.; Rehr, J. J.; Stern, E. A.; Yacoby, Y. *Physica B* **1995**, *208 & 209*, 154–156.

(28) McEwen, R. S. *J. Phys. Chem.* **1971**, *75*, 1782.

(29) Szytula, A.; Murasik, A.; Balanda, M. *Phys. Stat. Sol. B* **1971**, *43*, 125.

(30) Abrahams, S. C.; Bernstein, J. L. *Acta Crystallogr.* **1977**, *B33*, 3601–3604.

(31) Berendsen, H. J. C.; Grigera, J. R.; Straatsma, T. P. *J. Phys. Chem.* **1987**, *91*, 6269.

(32) Dang, L. X. *The parameters for bromine ion were supplied personally by Liem Dang,* 1997.

(33) Dang, L. X. *J. Am. Chem. Soc.* **1995**, *117*, 6954.

(34) Allen, M. P.; Tildesley, D. J. *Computer Simulation of Liquids*; Clarendon: Oxford, 1987.

(35) Palmer, B. J.; Garrett, B. C. *J. Chem. Phys.* **1993**, *98*, 4047.

(36) Dang, L. X.; Smith, D. E. *J. Chem. Phys.* **1995**, *102*, 3483.

(37) Waychunas, G. A.; Brown, G. E. *Phys. Chem. Miner.* **1990**, *17*, 420–430.

(38) Lever, A. B. P. *Inorganic Electronic Spectroscopy*, 2nd ed.; Elsevier: Amsterdam, 1984.

(39) Cotton, F. A.; Wilkinson, G. *Advanced Inorganic Chemisty*, 5th ed.; John Wiley and Sons: New York, 1988.

(40) Galoisy, L.; Calas, G. *Geochim. Cosmochim. Acta* **1993**, *57*, 3613–3626.

(41) Farges, F.; Brown, G. E. *Chem. Geol.* **1996**, *128*, 93–106.